Dalton Transactions

PAPER

View Article Online
View Journal | View Issue

Cite this: *Dalton Trans.*, 2026, **55**, 2111

Enhanced thermoelectric performance of flexible PEDOT:PSS/PEG matrices incorporating hollow Ag@Ag_2Se core–shell fillers

Oju Kwon,[a] Minsu Kim,[a] Jaeyeon Kim,[a] Jaekyung Lee,[a] Subin Lee,[b] Dabin Park[c] and Jooheon Kim *[a,b]

Flexible thermoelectric (TE) materials that can efficiently convert low-grade heat into electricity have received increasing attention for wearable and portable energy-harvesting systems. In this study, hollow Ag@Ag_2Se core–shell fillers were synthesized *via* a NaCl-templated method and incorporated into a PEDOT:PSS/PEG hybrid matrix to construct flexible TE composites. The hollow structure effectively reduced thermal transport through phonon scattering, while the metallic Ag core and semiconducting Ag_2Se shell provided continuous electron pathways and interfacial energy filtering. The addition of PEG improved interfacial compatibility and introduced thermal buffering behavior within the polymer network. As the filler content increased, both electrical conductivity and Seebeck coefficient were enhanced due to synergistic carrier transport between the hybrid phases. For the optimized composite containing 10 wt% hollow Ag@Ag_2Se, the maximum electrical conductivity of 41 913 S m^{-1} was achieved at 375 K, whereas the highest Seebeck coefficient of –151.5 μV K^{-1} and the maximum power factor of 876 μW m^{-1} K^{-2} were obtained at 300 K. Despite the increased electrical performance, the overall thermal conductivity remained as low as 0.4 W m^{-1} K^{-1}, resulting in a peak figure of merit (*ZT*) of 0.62. Moreover, the flexible device exhibited stable and reproducible output power of 3.8 μW at a temperature difference of 50 K. These results demonstrate that the combination of hollow Ag@Ag_2Se fillers and the PEDOT:PSS/PEG matrix provides an effective strategy for realizing high-performance, flexible thermoelectric materials suitable for low-grade waste heat recovery and wearable energy applications.

Received 25th November 2025,
Accepted 5th January 2026

DOI: 10.1039/d5dt02817e

rsc.li/dalton

1. Introduction

Thermoelectric (TE) materials capable of directly converting heat into electricity have attracted considerable attention for sustainable energy harvesting and waste-heat recovery applications.[1,2] However, the widespread use of inorganic TE materials such as Bi_2Te_3, PbTe, and SnSe is limited by their high cost, brittleness, and complicated fabrication processes. In contrast, organic or hybrid polymer-based TE materials have emerged as promising alternatives due to their low density, mechanical flexibility, solution processability, and low thermal conductivity.[3–5] Among them, poly(3,4-ethylenedioxythiophene):poly(styrenesulfonate) (PEDOT:PSS) has been widely studied because of its high electrical conductivity and environmental stability.[6–9] Nevertheless, its relatively low Seebeck coefficient and limited carrier mobility restrict further improvements in thermoelectric performance, defined by the dimensionless figure of merit

$$ZT = [S^2\sigma/\kappa] \times T \tag{1}$$

where S, σ, and κ denote the Seebeck coefficient, electrical conductivity, and thermal conductivity, respectively.

To overcome these limitations, numerous strategies such as secondary doping, hybridization with inorganic fillers, and interfacial engineering have been explored.[10,11] In particular, incorporating high-performance inorganic fillers into polymer matrices can enhance the carrier transport pathways and introduce energy-filtering effects that boost S without severely sacrificing σ. Among various inorganic candidates, silver selenide (Ag_2Se) has drawn significant attention as an n-type semiconductor with intrinsically high electrical conductivity and large Seebeck coefficient.[12,13] In addition, its relatively low toxicity and flexibility compared with traditional inorganic thermoelectrics make it suitable for hybrid systems. However, the dense nature of Ag_2Se and the interfacial mismatch with soft polymer matrices often lead to filler aggregation, poor dis-

---

[a] *School of Chemical Engineering, Chung-Ang University, Seoul 06974, Republic of Korea. E-mail: jooheonkim@cau.ac.kr*
[b] *Department of Intelligent Energy and Industry, Graduate School, Chung-Ang University, Seoul 06974, Republic of Korea*
[c] *Department of Mechanical and Aerospace Engineering, University of California, Irvine, CA 92679, USA*

persion, and thermal short-circuiting, which diminish the expected TE performance.

Recently, hollow or core–shell structured metallic fillers have been introduced to address these issues by simultaneously improving electrical conduction and suppressing heat transport.[14,15] The internal voids of hollow structures effectively scatter phonons and reduce thermal conductivity, while the metallic framework preserves high carrier mobility. Building upon this concept, constructing a hollow Ag@Ag_2Se core–shell filler can leverage the superior electrical transport of Ag and the semiconducting behavior of Ag_2Se to achieve a favorable balance between σ, S, and κ.

In this work, we report the synthesis of hollow Ag@Ag_2Se core–shell fillers *via* a NaCl-template-assisted method and their integration into a PEDOT:PSS/PEG hybrid matrix to form flexible thermoelectric composites. Polyethylene glycol (PEG) was introduced to enhance the interfacial compatibility between the polymer and the inorganic phase while simultaneously providing thermal buffering through its phase-change properties. The combination of a hollow metallic–semiconducting filler and a soft, conductive polymer matrix enables the design of a hybrid system with improved energy conversion efficiency and mechanical robustness. This study demonstrates that the synergistic interplay between the hollow Ag@Ag_2Se architecture and the PEDOT:PSS/PEG matrix leads to a remarkable enhancement in electrical conductivity, Seebeck coefficient, and power factor, while maintaining low thermal conductivity. Furthermore, the resulting flexible composite films exhibit stable thermoelectric power generation under practical temperature gradients, offering a promising pathway toward high-performance, lightweight, and wearable thermoelectric energy-harvesting devices.

2. Results and discussion

Fig. 1 shows a schematic illustration of the fabrication process of the hollow Ag@Ag_2Se/PEDOT:PSS/PEG composites. Hollow Ag particles were first synthesized using a NaCl-templated method, followed by an *in situ* Se^{2-} substitution reaction with Na_2SeSO_3 in diethylene glycol to form the Ag_2Se shell. In parallel, a conductive and thermally buffering polymer matrix was prepared by chemically incorporating PEG into PEDOT:PSS. Finally, the hollow Ag@Ag_2Se particles were dispersed into the polymer matrix and drop-cast into flexible films, enabling a synergistic design that combines high electrical conductivity, enhanced Seebeck coefficient, and reduced thermal conductivity.

2.1. Characterization of hollow Ag@Ag_2Se filler

Fig. 2 shows the morphological evolution of the samples. The pristine NaCl particles (Fig. 2a) exhibit irregular and nearly spherical shapes, whereas the NaCl templates (Fig. 2b) transformed into well-defined cubic crystals with smooth facets and uniform size, indicating successful shape control during the process. Particle size analysis was performed to quantitatively evaluate the size distribution and uniformity of the NaCl templates. As shown in Fig. S1, the differential particle size distribution exhibits a narrow and unimodal profile, indicating good uniformity of the NaCl templates. The cumulative distribution further confirms the limited size dispersion, suggesting that the template particles are well controlled. The mean particle size of the NaCl templates was determined to be approximately 1.93 μm. Such a uniform size distribution is beneficial for achieving reproducible hollow structures and plays a critical role in the subsequent formation and microstructural evolution of the hollow Ag and Ag@Ag_2Se structures. The hollow Ag particles (Fig. 2c) maintain this cubic framework but reveal a distinct internal cavity and partially opened edges, confirming the hollow structure. After surface modification, the hollow Ag@Ag_2Se particles (Fig. 2d) preserve the cubic outline while exhibiting a rougher surface, suggesting uniform coating and formation of a core–shell morphology. These observations confirm that each stage of transformation proceeds without loss of structural integrity, resulting in uniform hollow and

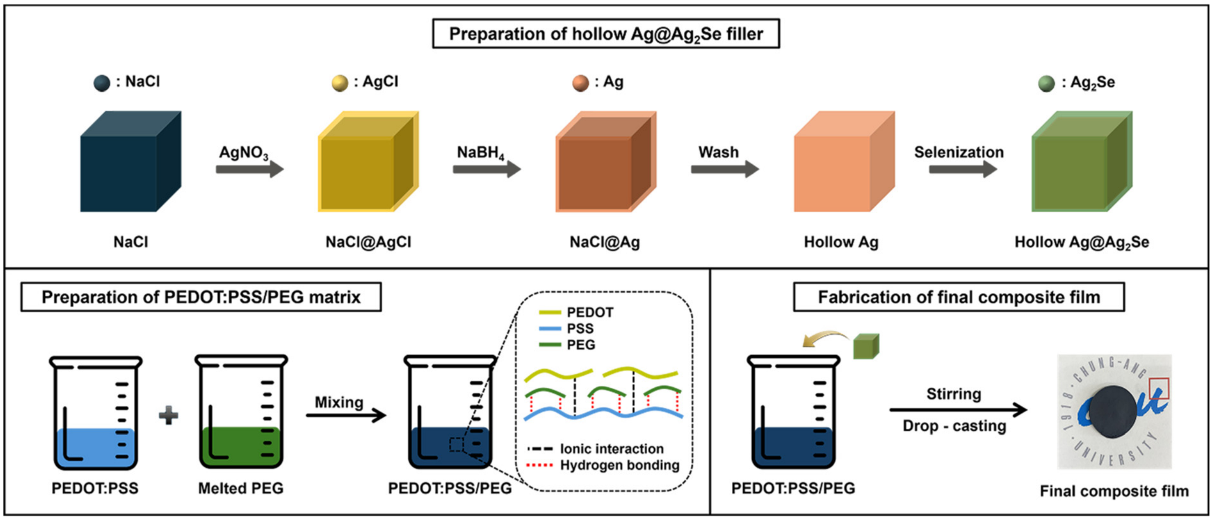

Fig. 1 Schematic illustration of the fabrication of the hollow Ag@Ag_2Se/PEDOT:PSS/PEG composite.

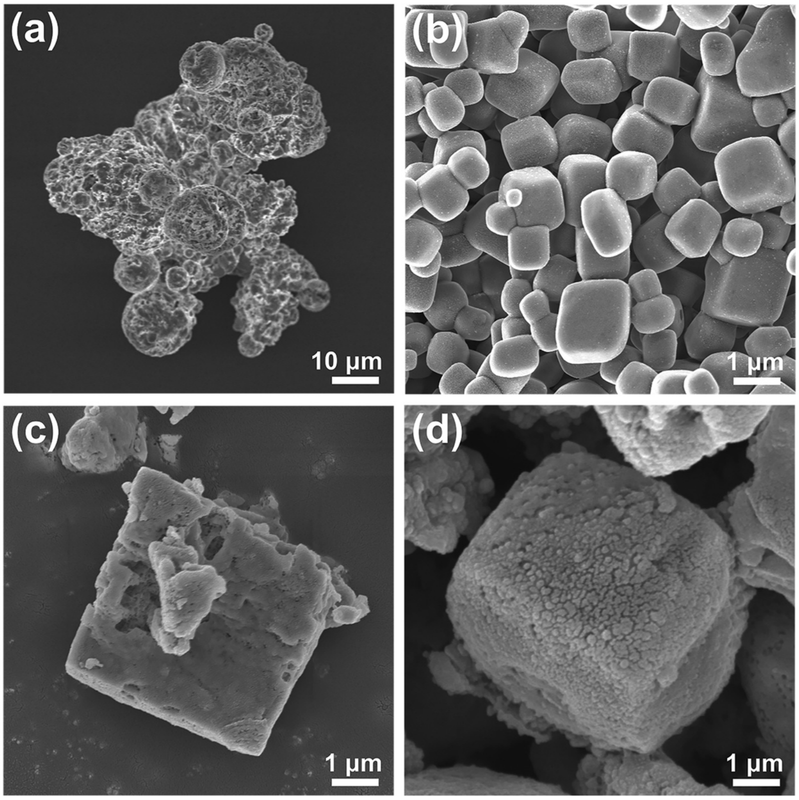

Fig. 2 Morphologies of (a) pristine NaCl, (b) NaCl template, (c) hollow Ag, and (d) hollow Ag@Ag_2Se.

core–shell architectures. As shown in Fig. S2a, the FE-SEM image clearly reveals the hollow architecture of the Ag@Ag_2Se particles, characterized by a well-defined internal cavity surrounded by a continuous shell. The corresponding EDS elemental mapping images (Fig. S2b and c) show that Ag and Se are uniformly distributed throughout the shell region. The presence of distinct shell–void interfaces and compositional confinement of Ag and Se to the outer framework indicate successful selenization of the hollow Ag template into hollow Ag@Ag_2Se, consistent with the proposed structural evolution.

The crystalline phases of the samples were identified by X-ray diffraction, as shown in Fig. 3a and b. Both pristine NaCl and the NaCl template (Fig. 3a) display diffraction peaks at 2θ = 27.3°, 31.7°, 45.5°, and 56.5°, which correspond well to the (111), (200), (220), and (222) planes of cubic NaCl (PDF # 00-005-0628). The identical peak positions and sharp intensities confirm that the templating process did not alter the crystallographic structure or crystallinity of NaCl.

In Fig. 3b, the diffraction pattern of hollow Ag exhibits reflections at 38.1°, 44.3°, and 64.4°, indexed to the (111), (200), and (220) planes of cubic Ag (PDF # 01-087-0717). After surface modification, additional peaks appear at 33.4°, 34.7°, 36.9°, and 39.9°, matching well with orthorhombic Ag_2Se (PDF # 01-080-7685). The coexistence of Ag and Ag_2Se diffraction peaks confirms the formation of a core–shell structure in which crystalline Ag_2Se is uniformly deposited on the hollow Ag surface without phase impurities.

The chemical states of the elements were further analyzed by X-ray photoelectron spectroscopy (Fig. 3c–f). The Ag 3d spectrum of hollow Ag (Fig. 3c) shows two peaks at 368.3 eV (Ag $3d_{5/2}$) and 374.3 eV (Ag $3d_{3/2}$), consistent with metallic Ag^0. Fig. 3d shows the XPS survey spectrum of the hollow Ag@Ag_2Se structure, where distinct Ag 3d and Se 3d signals are observed, along with minor O 1s and C 1s peaks attributed to surface-adsorbed species. Notably, no sulfur-related peaks are detected, indicating that sulfur is not incorporated into the final Ag@Ag_2Se structure. The atomic percentages derived from the survey spectrum further confirm that the composition is dominated by Ag and Se, supporting the formation of sulfur-free Ag@Ag_2Se rather than a mixed $Ag_2(S,Se)$ phase. In our synthesis, Na_2SO_3 was employed solely to generate the Na_2SeSO_3 selenium precursor by dissolving elemental Se in a sulfite solution, which is a well-established and widely adopted approach for solution-based Ag_2Se synthesis.[16,17] In this process, Na_2SO_3 functions as a reducing and complexing agent that facilitates the formation of reactive selenium species, rather than serving as a sulfur dopant source. In the case of hollow Ag@Ag_2Se (Fig. 3e), the Ag 3d peaks slightly shift toward higher binding energy and can be deconvoluted into Ag^0 and Ag^+ components, indicating partial oxidation of Ag and the presence of Ag–Se bonding. The Se 3d spectrum (Fig. 3f) exhibits characteristic doublets at 54.1 eV (Se $3d_{5/2}$) and 54.9 eV (Se $3d_{3/2}$), corresponding to Se^{2-} in Ag_2Se.[18–20] These results verify that Ag in the outer shell exists in a mixed

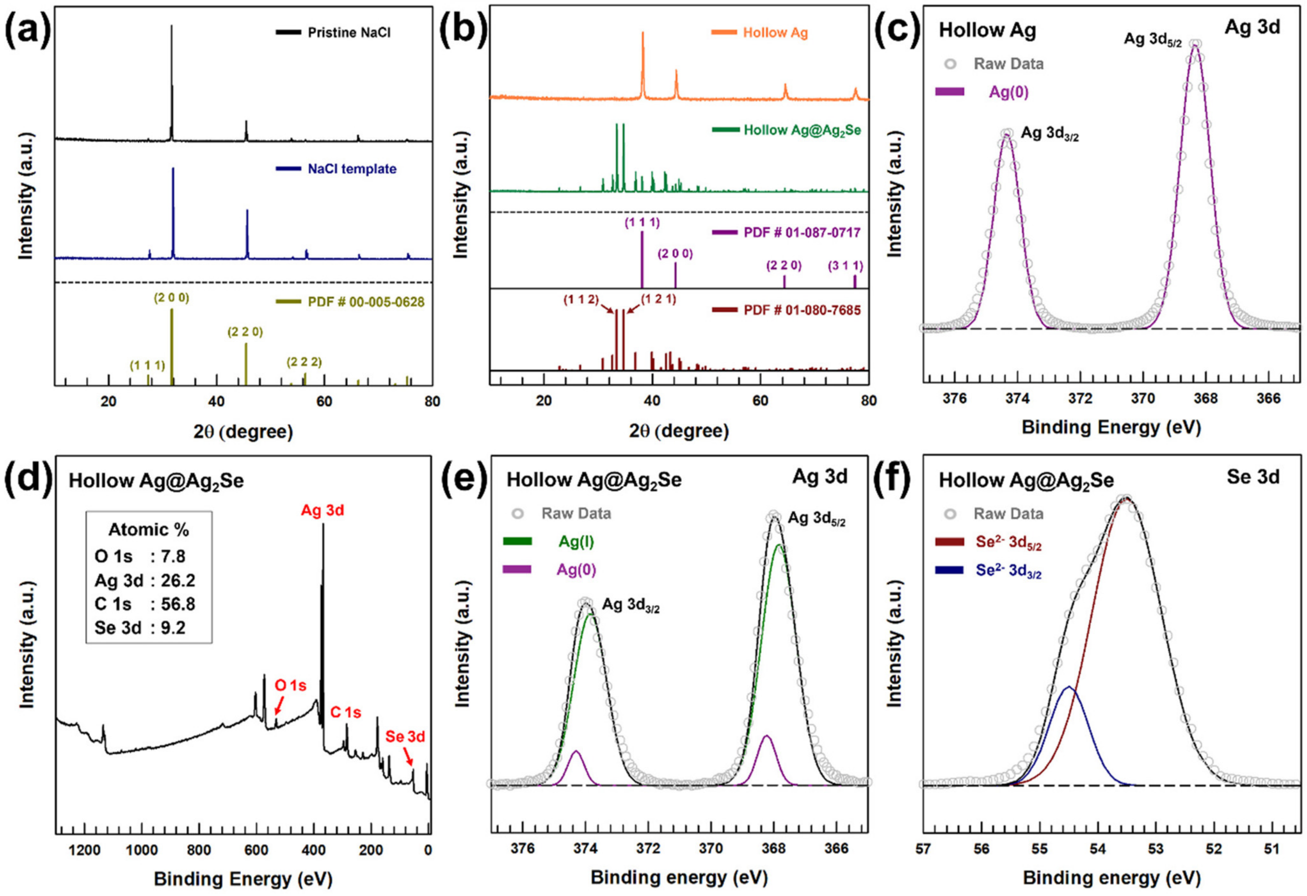

Fig. 3 XRD patterns of (a) pristine and prepared NaCl, and (b) hollow Ag and Ag@Ag_2Se. (d) XPS survey spectrum of Ag@Ag_2Se with an inset showing the atomic percentages. High-resolution XPS spectra of (c) hollow Ag and (e and f) hollow Ag@Ag_2Se.

valence state of Ag^0/Ag^+, while Se maintains the reduced Se^{2-} state, confirming the successful formation of the Ag_2Se phase on the hollow Ag framework.

2.2. Characterization of PEDOT:PSS/PEG matrix

Fig. 4 presents the structural and thermal analyses, as well as surface morphologies of the PEDOT:PSS/PEG matrix. The FT-IR spectra (Fig. 4a) reveal the characteristic peaks of each component. Pure PEG shows typical C–H stretching vibrations near 2880 cm^{-1} and a strong C–O–C stretching band at 1100 cm^{-1}, while PEDOT:PSS exhibits absorption bands associated with the C═C stretching of the thiophene ring (≈1510 cm^{-1}) and the S═O stretching of sulfonate groups (≈1130 cm^{-1}). In the PEDOT:PSS/PEG spectrum, the major peaks of both polymers are simultaneously observed, and a slight shift in the C–O–C and S═O bands indicates weak intermolecular interactions—likely hydrogen bonding—between PEG chains and PSS segments.[21,22] This suggests good miscibility and interfacial compatibility between the two components.

The DSC curves (Fig. 4b) show an endothermic peak for pure PEG corresponding to its melting transition at around 315 K. In the PEDOT:PSS/PEG composite, this melting peak shifts slightly to higher temperature and broadens, implying restricted crystallization of PEG within the polymer matrix and enhanced interfacial interaction with PEDOT:PSS.[23] Such thermal behavior demonstrates that PEG maintains its latent heat functionality while being partially confined by the conductive polymer network. Fig. S3 shows the variation in latent heat and electrical conductivity of the PEDOT:PSS/PEG matrix as a function of PEG1000 content. As the PEG content increased, the latent heat of the matrix increased monotonically, indicating enhanced phase-change behavior. In contrast, the electrical conductivity decreased with increasing PEG content, reflecting the insulating nature of PEG and the disruption of continuous PEDOT:PSS conductive pathways at higher loadings. These results reveal a clear trade-off between latent heat performance and electrical transport. Notably, a PEG1000 content of 10 wt% provided a distinct latent heat (~20 J g^{-1}) while retaining relatively high electrical conductivity compared to higher PEG loadings. Therefore, considering the balance between achieving meaningful latent heat performance and minimizing electrical conductivity deterioration, 10 wt% PEG1000 was selected as the optimal composition for this study.

The SEM images (Fig. 4c–e) further illustrate the morphological differences among the matrices. Pure PEDOT:PSS (Fig. 4c)

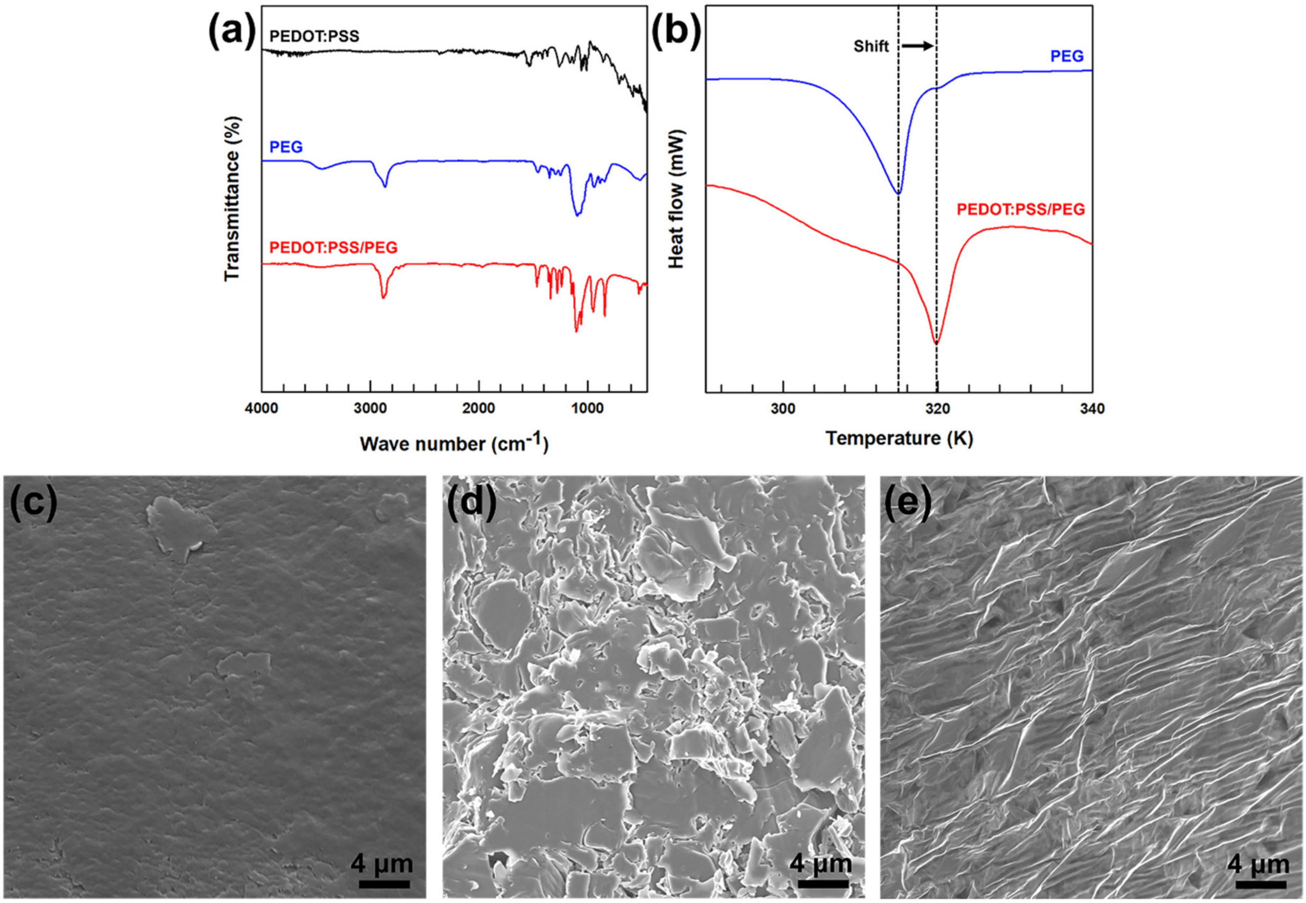

Fig. 4 (a) FT-IR spectra and (b) DSC curves of the matrices during the preparation of PEDOT:PSS/PEG. Morphologies of (c) pure PEDOT:PSS, (d) PEG, and (e) PEDOT:PSS/PEG.

exhibits a relatively smooth and dense surface, whereas PEG (Fig. 4d) shows a rough and fractured morphology due to its crystalline nature. In contrast, the PEDOT:PSS/PEG composite (Fig. 4e) displays an interconnected, wrinkled texture, suggesting the formation of a continuous mixed phase. The wrinkled and layered surface structure is beneficial for flexible thermoelectric applications, as it enhances mechanical compliance and provides continuous electron transport pathways through the PEDOT:PSS framework.

2.3. Characterization of final composite film

Fig. 5 shows the macroscopic and microscopic morphologies of the PEDOT:PSS/PEG matrices incorporating different loadings of hollow Ag@Ag_2Se fillers. The digital photograph in Fig. 5a demonstrates that the final composite forms a flexible, free-standing film with a uniform black appearance and smooth surface, confirming good film integrity and homogeneity over a large area.

Cross-sectional FE-SEM images (Fig. 5b–e) reveal the dispersion behavior of the hollow Ag@Ag_2Se fillers within the polymer matrix at various concentrations. At 2.5 wt% loading (Fig. 5b), a small number of isolated filler particles are sparsely embedded within the dense polymer network. Increasing the filler content to 5 wt% (Fig. 5c) results in a more uniform distribution with minimal interfacial voids, suggesting improved compatibility between the inorganic fillers and the organic matrix. At 7.5 wt% (Fig. 5d), the fillers are well interconnected while still maintaining a continuous polymeric phase, forming a percolated microstructure that can facilitate efficient charge transport. However, at 10 wt% loading (Fig. 5e), partial aggregation of fillers becomes apparent, with densely packed clusters observed throughout the cross section. At Ag@Ag_2Se loadings above 10 wt%, severe filler aggregation and loss of film-forming ability prevented the fabrication of continuous composite films, imposing a practical upper limit on the filler content in this system.

The elemental mapping images (Fig. 5f) further confirm the presence and homogeneous distribution of Ag and Se within the composite, corresponding to the hollow Ag@Ag_2Se phase, while the C signal originates from the PEDOT:PSS/PEG matrix. The co-localization of Ag and Se signals without significant segregation verifies that the fillers are evenly dispersed and maintain their core–shell composition within the polymer framework.

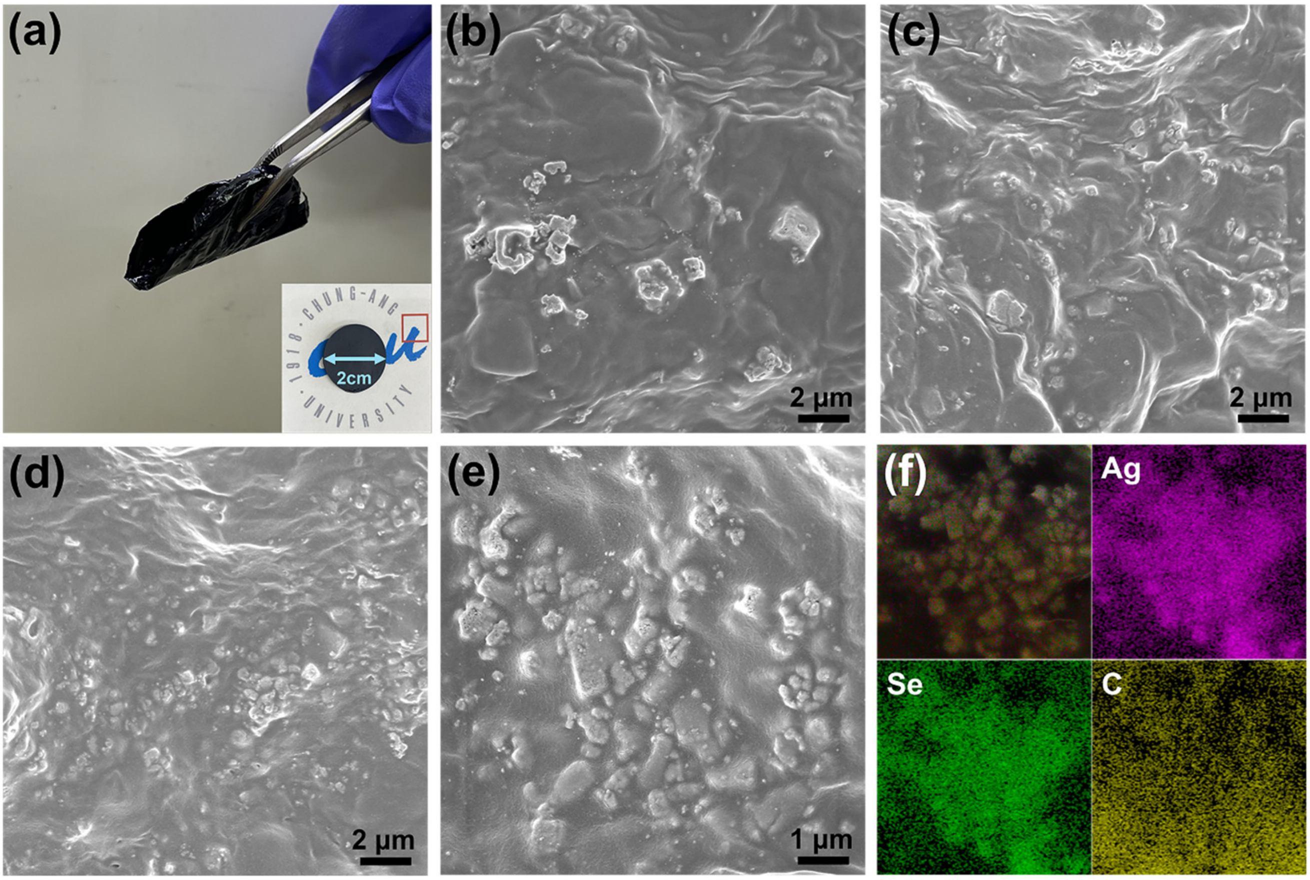

Fig. 5 (a) Digital photograph of the final composite and the inset shows the top surface of composite. Cross-sectional FE-SEM images of composite using (b) 2.5 wt%, (c) 5 wt%, (d) 7.5 wt%, and (e) 10 wt% of filler. (f) EDS elemental mapping images of final composite.

2.4. Thermoelectrical properties of composite film

Fig. 6 presents the temperature-dependent electrical transport properties of the PEDOT:PSS/PEG composites with different Ag@Ag_2Se filler contents. As shown in Fig. 6a, the electrical conductivity increases monotonically with increasing filler loading across the entire temperature range, indicating that the incorporation of Ag@Ag_2Se effectively promotes charge transport within the composite. This enhancement can be attributed to the formation of percolated conductive pathways through the Ag core and the efficient carrier transport enabled by the semiconducting Ag_2Se shell.[24–26] The 10 wt% composite exhibits the highest electrical conductivity (41 913 S m^{-1}), which is attributed to the formation of interconnected conducting pathways through the Ag@Ag_2Se fillers and improved interfacial charge transport between the inorganic and polymeric phases. In addition, all composites exhibit a conductivity maximum at approximately 375 K, which reflects the interplay between thermally activated carrier generation and mobility degradation at elevated temperatures.[27,28]

To further analyze, the electrical conductivity and Seebeck coefficient can be expressed using the following equations:

$$\sigma = n \times e \times \mu \tag{2}$$

$$S = \frac{8 \times \pi^2 \times {k_B}^2}{3 \times e \times h^2} \times m^* \times T \times \left(\frac{\pi}{3 \times n}\right)^{\frac{2}{3}} \tag{3}$$

where n, e, μ, k_B, h, and m^* denote the carrier concentration, electron charge, carrier mobility, Boltzmann's constant, Planck's constant, and effective mass of the carrier, respectively.[29] Based on eqn (2), the increase in electrical conductivity with filler content can be directly correlated with the enhanced carrier concentration and the establishment of additional conductive pathways. This interpretation is further supported by Fig. 6b, which shows that the carrier concentration of the 10 wt% composite increases steadily with temperature, indicating enhanced thermal activation of charge carriers and effective carrier injection from the Ag@Ag_2Se fillers into the polymer matrix. Conversely, the carrier mobility decreases with increasing temperature due to intensified carrier–phonon scattering and structural disorder. The observed conductivity maximum around 375 K therefore arises from the competition between increasing carrier concentration and decreasing mobility, with carrier activation dominating at intermediate temperatures.

The Seebeck coefficient behavior shown in Fig. 6c can also be rationalized using eqn (3). The absolute value of the Seebeck coefficient increases with increasing Ag@Ag_2Se

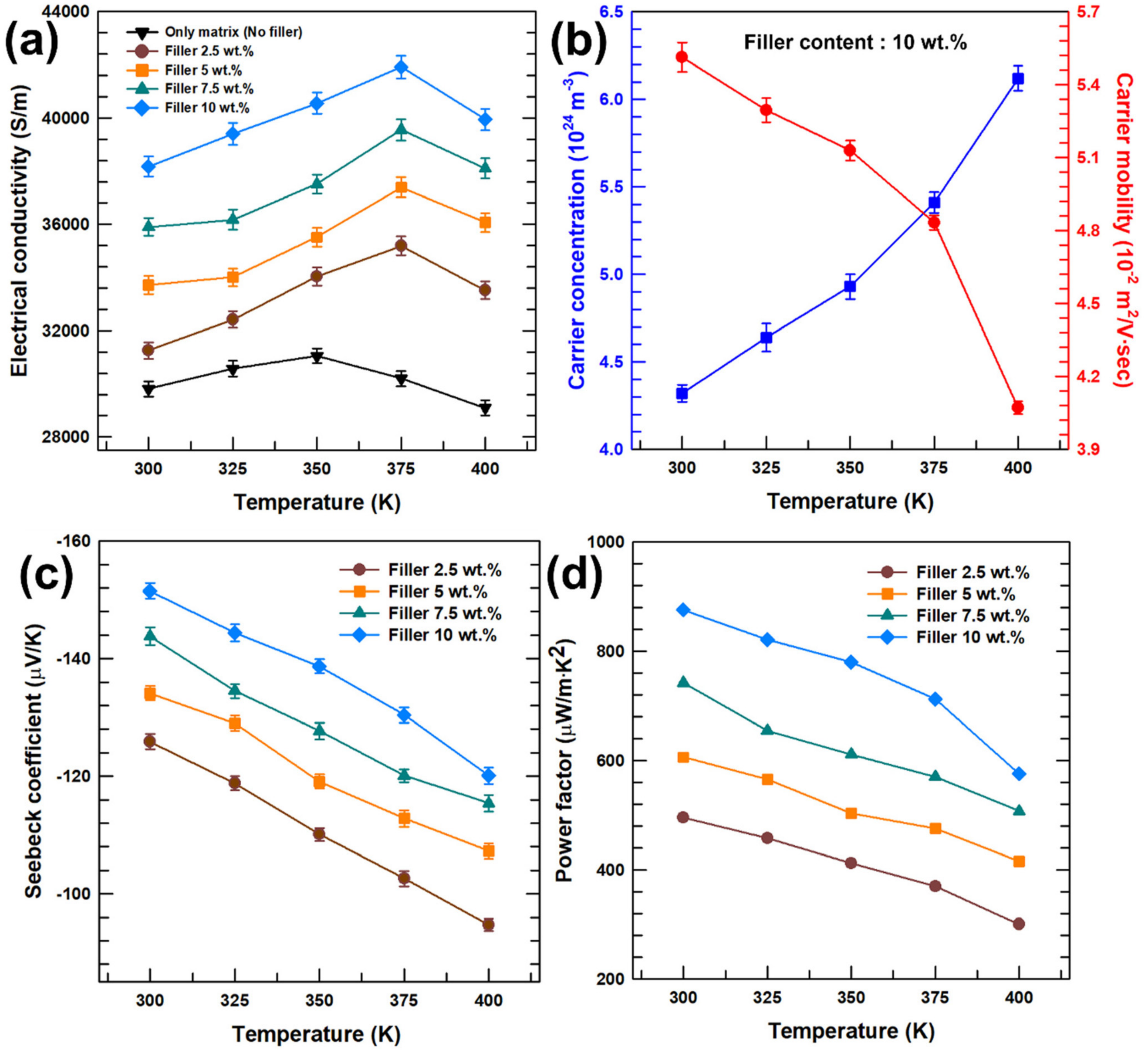

Fig. 6 Temperature-dependent (a) electrical conductivity, (b) carrier concentration and mobility, (c) Seebeck coefficient, and (d) power factor of each composite.

content, reflecting the dominant contribution of the n-type Ag_2Se shell to the overall thermopower of the composite.[30,31] According to eqn (3), an increase in carrier concentration leads to a reduction in the Seebeck coefficient, which explains the gradual decrease in $|S|$ with increasing temperature as carrier concentration increases. This behavior is consistent with the typical trade-off between electrical conductivity and thermopower in thermoelectric materials.

Consequently, the power factor (PF) shown in Fig. 6d exhibits a combined dependence on electrical conductivity and Seebeck coefficient. The 10 wt% composite achieves the highest power factor of 876.2 $\mu W\ m^{-1}\ K^{-2}$ at 300 K, representing an approximately 86-fold enhancement compared to the pristine PEDOT:PSS/PEG matrix without $Ag@Ag_2Se$ fillers (10.2 $\mu W\ m^{-1}\ K^{-2}$). This improvement demonstrates the synergistic effect of the highly conductive Ag core and the semiconducting Ag_2Se shell within the flexible PEDOT:PSS/PEG matrix. Overall, these results confirm that the incorporation of an optimal amount of hollow $Ag@Ag_2Se$ fillers significantly enhances charge carrier transport and thermoelectric performance while maintaining stable temperature dependence.

Fig. 7a shows the temperature-dependent thermal conductivity (κ) of the PEDOT:PSS/PEG composites with different $Ag@Ag_2Se$ filler contents. The thermal conductivity increases gradually with increasing filler loading over the entire temperature range, which is primarily attributed to the intrinsically

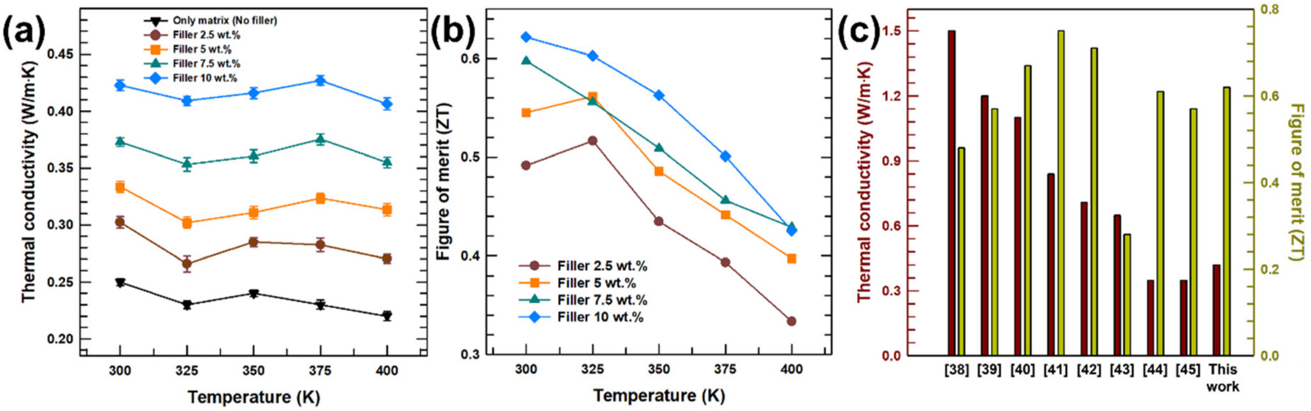

Fig. 7 Temperature-dependent (a) thermal conductivity and (b) figure-of-merit of each composite. (c) Comparison of thermal conductivity and figure-of-merit at 300 K with other previous studies.

higher thermal conductivity of the Ag@Ag_2Se fillers compared to the polymer matrix. Nevertheless, the overall κ values remain relatively low (<0.45 W m^{-1} K^{-1} even at 10 wt%), indicating that phonon transport is effectively suppressed by the polymer-rich matrix and abundant polymer–inorganic interfaces.[32] The weak temperature dependence of κ further suggests that phonon-dominated heat transport governs the thermal conduction behavior of the composites.

The thermoelectric properties of the pristine PEDOT:PSS/PEG matrix were examined to provide a reference for comparison with the Ag@Ag_2Se-containing composites. As shown in Fig. 6a and 7a, the electrical conductivity and thermal conductivity of the PEDOT:PSS/PEG matrix are comparable to those of the final composites over the measured temperature range, indicating that the polymer matrix itself provides continuous electrical transport pathways and a low thermal conductivity framework. However, as summarized in Table S1, the Seebeck coefficient of the PEDOT:PSS/PEG matrix is very low and decreases with increasing temperature, which results in extremely small power factor and figure of merit values. These results demonstrate that, despite favorable electrical and thermal transport properties, the intrinsic thermoelectric performance of the PEDOT:PSS/PEG matrix is limited by its low thermopower. Consequently, the significant enhancement in thermoelectric performance observed in the composites is primarily attributed to the incorporation of Ag@Ag_2Se fillers rather than the polymer matrix itself.

To further analyze this trend, the total thermal conductivity (κ), electronic thermal conductivity (κ_e) and Lorentz number (L) can be expressed using the following equations:

$$\kappa = \kappa_e + \kappa_l \tag{4}$$

$$\kappa_e = L \times T \times \sigma \tag{5}$$

$$L = \left[1.5 + \exp\left(-\frac{|S|}{116}\right)\right] \times 10^{-8} \tag{6}$$

where κ_l, T, σ, and S denote the lattice thermal conductivity, absolute temperature, electrical conductivity, and Seebeck coefficient, respectively.[33,34] Based on the measured Seebeck coefficient and electrical conductivity, the L, κ_e, and κ_l values calculated at 300 K are presented in Fig. S4. As shown in Fig. S4, the κ_e increases with both temperature and filler loading and is substantially higher than the κ_l over the entire temperature range. The κ_l remains markedly suppressed because the designed polymer–inorganic interfaces and hollow architectures effectively scatter phonons, thereby limiting lattice-mediated heat transport. These interfaces, intentionally introduced to disrupt phonon propagation, ensure that phonon transport is strongly hindered and that the lattice contribution remains minimal even at higher filler loadings.[35,36] As a result, the κ_e becomes the dominant component of the total thermal conductivity. This pronounced dominance of κ_e originates from the highly conductive Ag core and the semiconducting Ag_2Se shell, which together form continuous and percolated pathways for charge carriers, thereby enhancing carrier-mediated heat transport in accordance with the Wiedemann–Franz relation.[11,37]

Fig. 7b presents the temperature-dependent figure of merit (ZT) for the composites. Despite the moderate increase in thermal conductivity with increasing filler content, the ZT values are significantly enhanced at higher Ag@Ag_2Se loadings. This improvement arises from the substantial enhancement in power factor, which outweighs the unfavorable effect of increased κ. The 10 wt% composite exhibits the highest ZT across the entire temperature range, demonstrating that the optimized balance between electrical transport and thermal conduction is achieved at this filler content. The gradual decrease in ZT with increasing temperature is mainly attributed to the reduction in power factor, as discussed in Fig. 6, rather than to changes in thermal conductivity.

Fig. 7c compares the thermal conductivity and ZT values of the present composites at 300 K with those reported in previous studies.[38–45] The hollow Ag@Ag_2Se/PEDOT:PSS/PEG system demonstrates a substantially lower κ and a comparable or higher

ZT than most polymer-based thermoelectric composites, highlighting the effectiveness of integrating hollow metallic–semiconducting fillers within a flexible organic matrix. These results suggest that the designed composite structure successfully achieves a favorable balance between electrical and thermal transport, rendering it a promising candidate for flexible and energy-efficient thermoelectric applications.

To evaluate the thermal-cycle stability of the optimized composite, the thermoelectric properties of the 10 wt% Ag@Ag_2Se/PEDOT:PSS/PEG composite were measured after repeated heating–cooling cycles between 300 and 400 K (Table S2). As the number of cycles increased from 0 to 20, the electrical conductivity exhibited a gradual decrease from 38 174 to 36 019 S m^{-1}. This moderate reduction is attributed to minor rearrangements at the filler–polymer interfaces and slight relaxation of percolated conductive pathways induced by thermal cycling. In contrast, the Seebeck coefficient remained highly stable, showing only a marginal change from −151.5 to −149.1 μV K^{-1} after 20 cycles. Meanwhile, the thermal conductivity remained nearly unchanged, with values fluctuating within a narrow range of 0.42–0.43 W m^{-1} K^{-1}, suggesting that the phonon transport characteristics and interfacial phonon-scattering structures are well maintained. Overall, the minimal variations in electrical conductivity, Seebeck coefficient, and thermal conductivity demonstrate that the Ag@Ag_2Se/PEDOT:PSS/PEG composite possesses good thermal-cycle stability and repeatability, supporting the reliability of the observed thermoelectric performance under repeated heating–cooling conditions relevant to practical operation.

Fig. S5 presents the environmental stability of the optimized composite containing 10 wt% Ag@Ag_2Se fillers, evaluated by monitoring the time-dependent thermoelectric properties under humid air conditions (RH 70%) at 300 K. As shown in Fig. S5a, the electrical conductivity exhibits a gradual and limited decrease over 14 days, retaining 94.1% of its initial value. This slight reduction can be attributed to mild humidity- and air-induced interfacial relaxation within the polymer–inorganic composite, while the overall conductive network remains well preserved. The Seebeck coefficient (Fig. S5b) shows only a minor decrease in its absolute value during the same period, with a retention exceeding 95%. The relatively stable Seebeck response indicates that the dominant carrier transport mechanism and the energy-filtering effect at the Ag@Ag_2Se–polymer interfaces are largely maintained despite prolonged exposure to humid air.[46] In contrast to the electrical conductivity, the Seebeck coefficient is less sensitive to interfacial relaxation and environmental perturbations, resulting in enhanced stability. As shown in Fig. S5c, the thermal conductivity remains nearly constant, with only a marginal increase (<3%) over 14 days. This behavior suggests that heat transport is primarily governed by the polymer matrix and the hollow filler architecture, and that phonon scattering mechanisms are not significantly altered by environmental exposure. The negligible change in thermal conductivity further confirms the structural integrity of the composite under humid air conditions.

Overall, the results demonstrate that the optimized Ag@Ag_2Se/PEDOT:PSS/PEG composite exhibits good environmental stability, with minimal degradation in electrical, thermoelectric, and thermal transport properties over time. These findings indicate that the composite is resistant to combined humidity and oxidative environments relevant to practical operation, supporting its potential applicability in flexible thermoelectric devices.

The thermoelectric output characteristics of the final composite device were evaluated under different temperature gradients, as shown in Fig. 8. The voltage–current (*V*–*I*) curves (Fig. 8a) exhibit a linear relationship at all temperature differences (ΔT = 10–50 K), confirming the ohmic behavior of the composite film and stable carrier transport across the device. The open-circuit voltage (V_{OC}) increases proportionally with ΔT, indicating a consistent Seebeck response. The inset of Fig. 8a compares the measured and calculated V_{OC} values, which show nearly identical slopes, verifying the reliability of the experimental results and the reproducibility of the thermoelectric effect. Under ΔT conditions of 30 and 40 K, the open-circuit voltages were found to be 21.6 and 28.8 mV, respectively, which straighten well with the theoretical predictions based on the equation:

$$V_{\mathrm{OC}} = N \times |S| \times \Delta T \tag{7}$$

Here, *N* represents the total number of thermoelectric legs (*N* = 6 in this study).[47,48] By applying this formula, the estimated V_{OC} for ΔT = 40 K is around 30.3 mV, which shows good agreement with the experimentally obtained result. The slight reduction in the measured V_{OC} compared to the theoretically predicted value can be attributed to thermal contact losses and the temperature-dependent nature of the Seebeck coefficient. Due to thermal resistance at the hot-side block, polyimide substrate, and Ag-paste junctions, the actual temperature difference across the legs is smaller than the set ΔT value. Moreover, while the theoretical V_{OC} was calculated using the Seebeck coefficient measured at 300 K, the actual *S* value tends to decrease with increasing temperature.[49] As a result, these experimental factors lead to a lower measured V_{OC} than the theoretical prediction.

The corresponding power–current (*P*–*I*) characteristics (Fig. 8b) show parabolic trends typical of thermoelectric generators, where power output increases with current, reaches a maximum, and then decreases as resistive losses dominate. The *P* is calculated using the following expression:

$$P = \left(\frac{V_{\mathrm{OC}}}{R_{\mathrm{load}} + R_{\mathrm{in}}}\right)^2 \times R_{\mathrm{load}} \tag{8}$$

where R_{in} is the internal resistance, and R_{load} is the load resistance of the TEG. The maximum power output is achieved when R_{in} equals R_{load}.[50] The maximum output power (P_{max}) systematically increases with the applied temperature difference, reaching approximately 3.8 μW at ΔT = 50 K. This enhancement reflects the combined effect of the improved electrical conductivity and high Seebeck coefficient of the composite, which together facilitate efficient conversion of thermal energy into electrical power.

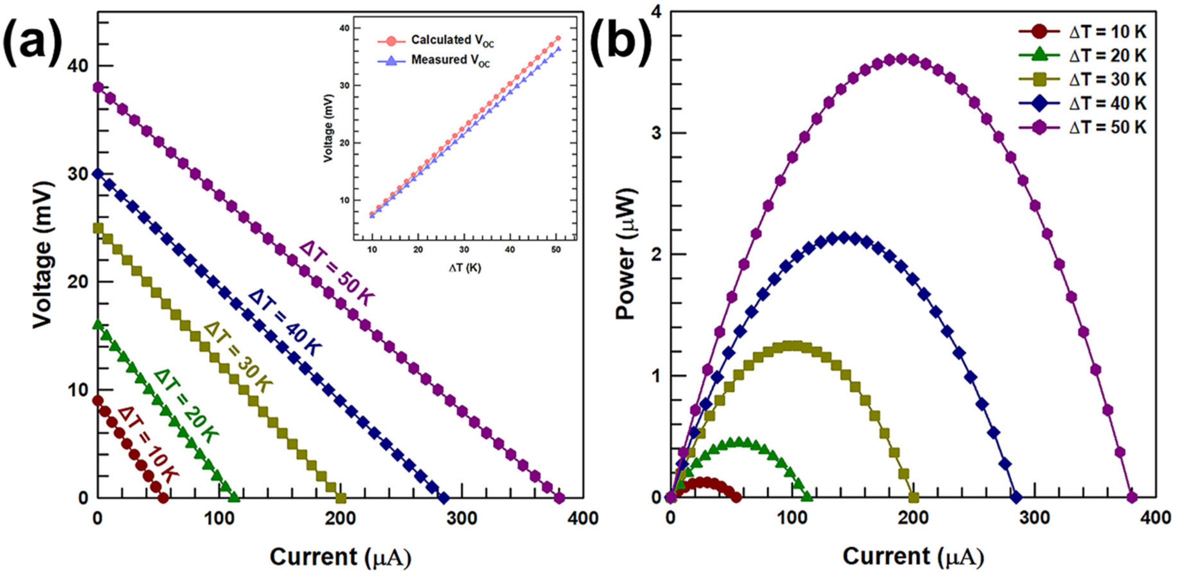

Fig. 8 (a) Output voltage and (b) power as functions of current at various temperature differences. The inset shows calculated and measured open-circuit voltage.

Overall, these results confirm that the flexible hollow Ag@Ag_2Se/PEDOT:PSS/PEG composite device exhibits stable and reproducible thermoelectric performance under varying temperature gradients, demonstrating its potential applicability for low-grade waste heat harvesting and flexible energy generation systems.[51]

3. Conclusions

In this study, flexible thermoelectric composites based on a PEDOT:PSS/PEG matrix and hollow Ag@Ag_2Se core–shell fillers were successfully fabricated through a solution-processable approach. The NaCl-templated method enabled the synthesis of well-defined hollow Ag particles, and subsequent selenization produced uniform Ag_2Se shells while preserving the cubic morphology. The conductive polymer matrix, modified with PEG, exhibited enhanced interfacial compatibility and latent-heat buffering characteristics, which effectively stabilized the composite microstructure.

The incorporation of hollow Ag@Ag_2Se fillers significantly improved the thermoelectric performance of the composites. The 10 wt% sample achieved an electrical conductivity of 41 913 S m^{-1} and a Seebeck coefficient of −151.5 μV K^{-1}, leading to a maximum power factor of 876 μW m^{-1} K^{-2}. Despite the high filler loading, the overall thermal conductivity remained low (≈0.4 W m^{-1} K^{-1}), owing to phonon scattering at the polymer–inorganic interfaces and the hollow interior structure of the fillers. Consequently, a peak figure of merit (ZT) of 0.62 was obtained at 300 K, surpassing most previously reported polymer-based thermoelectric systems. Furthermore, the flexible device demonstrated stable and reproducible output characteristics, generating an open-circuit voltage of ~40 mV and a maximum power of ~3.8 μW at a temperature gradient of 50 K. These results highlight the synergistic effects of the conductive polymer network, thermally adaptive PEG phase, and hollow Ag@Ag_2Se architecture.

Overall, this work provides a simple and effective strategy for designing hybrid thermoelectric composites that combine high electrical conductivity, low thermal conductivity, and mechanical flexibility. The proposed system shows strong potential for low-grade waste heat recovery and wearable energy-harvesting applications.

Conflicts of interest

There are no conflicts to declare.

Data availability

All the data used are included in the manuscript, if raw data is needed it will be provided upon requesting the corresponding author.

Supplementary information (SI) is available. See DOI: https://doi.org/10.1039/d5dt02817e.

Acknowledgements

This work was supported by the Technology Innovation Program(RS-2024-00421213, Heat Dissipation Control Technology Development for High-Current Busbar Connection Components) funded By the Ministry of Trade Industry & Energy(MOTIE, Korea) and supported by Korea Institute for Advancement of Technology (KIAT) grant funded by the Korea

Government (MOTIE) (RS-2025-02263458, HRD Program for Industrial Innovation).

References

1 H. Han, L. Zhao, X. Wu, B. Zuo, S. Bian, T. Li, X. Liu, Y. Jiang, C. Chen and J. Bi, *J. Mater. Chem. A*, 2024, **12**, 24041–24083.

2 X.-L. Shi, J. Zou and Z.-G. Chen, *Chem. Rev.*, 2020, **120**, 7399–7515.

3 N. Nandihalli, C.-J. Liu and T. Mori, *Nano Energy*, 2020, **78**, 105186.

4 Y. Du, S. Z. Shen, K. Cai and P. S. Casey, *Prog. Polym. Sci.*, 2012, **37**, 820–841.

5 M. H. Lin, M. G. Mohamed, C. J. Lin, Y. J. Sheng, S. W. Kuo and C. L. Liu, *Adv. Funct. Mater.*, 2024, **34**, 2406165.

6 O. Kwon, M. Kim, J. Lee, S. Lee, J. Kim, M. Kim and J. Kim, *J. Alloys Compd.*, 2025, **1014**, 178789.

7 Y. Zhang, Y. Zhang, W. Deng, Q. Li, M. Guo and G. Chen, *Adv. Funct. Mater.*, 2025, **35**, 2420644.

8 S. Liu, H. Li, X. Fan and C. He, *Compos. Sci. Technol.*, 2022, **221**, 109347.

9 N. Wen, X. Guan, X. Zuo, Y. Guo, Z. Chen, C. Li, H. Xu, L. Pan and Z. Fan, *Adv. Funct. Mater.*, 2024, **34**, 2315677.

10 D.-h. Kim, S. Shin, S.-j. Jeon and S. Han, *J. Alloys Compd.*, 2025, **1010**, 177095.

11 Z. Wehbi, R. Taher, J. Faraj, C. Castelain and M. Khaled, *Energy Rep.*, 2022, **8**, 1361–1370.

12 D. Park, H. Ju and J. Kim, *J. Ind. Eng. Chem.*, 2021, **93**, 333–338.

13 H. Wu, X.-l. Shi, J. Duan, Q. Liu and Z.-G. Chen, *Energy Environ. Sci.*, 2023, **16**, 1870–1906.

14 R. Mulla and C. W. Dunnill, *Mater. Adv.*, 2022, **3**, 125–141.

15 M. Ibanez, R. Zamani, S. Gorsse, J. Fan, S. Ortega, D. Cadavid, J. R. Morante, J. Arbiol and A. Cabot, *ACS Nano*, 2013, **7**, 2573–2586.

16 Y.-l. Yan, X.-f. Qian, H.-j. Xu, J. Yin and Z.-k. Zhu, *Inorg. Chem. Commun.*, 2003, **6**, 34–37.

17 P. P. J. Helan, K. Mohanraj and G. Sivakumar, *Trans. Nonferrous Met. Soc. China*, 2015, **25**, 2241–2246.

18 D. Park, M. Kim and J. Kim, *Adv. Electron. Mater.*, 2024, **10**, 2400018.

19 X. Li, Y. Lu, K. Cai, M. Gao, Y. Li, Z. Wang, M. Wu, P. Wei, W. Zhao and Y. Du, *Chem. Eng. J.*, 2022, **434**, 134739.

20 F. Sun, Y. Li, Z. Wu, Y. Liu, H. Tang, X. Li, Z. Yue and L. Zhou, *RSC Adv.*, 2018, **8**, 32808–32813.

21 J. M. Yun, J. S. Yeo, J. Kim, H. G. Jeong, D. Y. Kim, Y. J. Noh, S. S. Kim, B. C. Ku and S. I. Na, *Adv. Mater.*, 2011, **23**, 4923–4928.

22 J. Lee and J. Kim, *Mater. Today Chem.*, 2023, **27**, 101305.

23 M. Wintersgill, J. Fontanella, P. Stallworth, S. Newman, S. H. Chung and S. Greenbaum, *Solid State Ionics*, 2000, **135**, 155–161.

24 L. Wang, P. Miao, X.-L. Shi, L. Li, Z. Shen, L. Huang, Z.-G. Chen, J. Ding and N. Yuan, *J. Alloys Compd.*, 2025, 181456.

25 H. Chen, X. Xiang, M. Xu, Y. Zhao, W. Sun, X. Ren, S. Xue, S. Li, Y. Li and X. Zu, *J. Alloys Compd.*, 2025, 182586.

26 T. A. Yemata, A. K. K. Kyaw, Y. Zheng, J. Xu, W. S. Chin, Q. Zhu and Y. Hayashi, *J. Mater. Chem. A*, 2025, **13**, 35976–35998.

27 O. Kwon, M. Kim, J. Kim, J. Lee, S. Lee, J. Lee and J. Kim, *CrystEngComm*, 2025, **27**, 5173–5183.

28 L. Su, H. Shi, S. Wang, D. Wang, B. Qin, Y. Wang, C. Chang and L. D. Zhao, *Adv. Energy Mater.*, 2023, **13**, 2300312.

29 H. Ju and J. Kim, *ACS Nano*, 2016, **10**, 5730–5739.

30 D. Ji, B. Li, X. Li, H. H. AlTakrori, B. Thirumalraj, M. d. Rezeq, W. Cantwell and L. Zheng, *Adv. Sci.*, 2025, e08381.

31 D. Theprattanakorn, T. Kaewmaraya and S. Pinitsoontorn, *Adv. Mater. Technol.*, 2025, **10**, e00093.

32 Z. Chen, C. Yu, Y. Ge, K. Ou, J. Chen and H. Lu, *Chem. Eng. J.*, 2024, **500**, 156924.

33 H.-S. Kim, Z. M. Gibbs, Y. Tang, H. Wang and G. J. Snyder, *APL Mater.*, 2015, 3.

34 M. Saif and D. Tripathi, *Energy Storage*, 2024, **6**, e545.

35 R. Abinaya, J. Archana, S. Harish, M. Navaneethan, C. Muthamizhchelvan, S. Ponnusamy, H. Udono, R. Sugahara, Y. Hayakawa and M. Shimomura, *J. Colloid Interface Sci.*, 2021, **584**, 295–309.

36 M. A. Jenisha, S. Harish, J. Archana and M. Navaneethan, *J. Alloys Compd.*, 2025, 184493.

37 Q. Cheng, H. Sun, Z. Yu, G. Luo, Y. Qi, Y. Yuan, B. Huang, Y. Wang and H. Zhou, *Nano Energy*, 2025, 111560.

38 T. Day, F. Drymiotis, T. Zhang, D. Rhodes, X. Shi, L. Chen and G. J. Snyder, *J. Mater. Chem. C*, 2013, **1**, 7568–7573.

39 P. Jood, R. Chetty and M. Ohta, *J. Mater. Chem. A*, 2020, **8**, 13024–13037.

40 H. Duan, Y. Li, K. Zhao, P. Qiu, X. Shi and L. Chen, *JOM*, 2016, **68**, 2659–2665.

41 T. Kleinhanns, F. Milillo, M. Calcabrini, C. Fiedler, S. Horta, D. Balazs, M. J. Strumolo, R. Hasler, J. Llorca and M. Tkadletz, *Adv. Energy Mater.*, 2024, **14**, 2400408.

42 C. Jiang, Y. Ding, K. Cai, L. Tong, Y. Lu, W. Zhao and P. Wei, *ACS Appl. Mater. Interfaces*, 2020, **12**, 9646–9655.

43 C. Lee, Y.-H. Park and H. Hashimoto, *J. Appl. Phys.*, 2007, 101.

44 J. Chen, Q. Sun, D. Bao, T. Liu, W.-D. Liu, C. Liu, J. Tang, D. Zhou, L. Yang and Z.-G. Chen, *ACS Appl. Mater. Interfaces*, 2020, **12**, 51523–51529.

45 M. M. Mallick, A. G. Rösch, L. Franke, S. Ahmed, A. Gall, H. Geßwein, J. Aghassi and U. Lemmer, *ACS Appl. Mater. Interfaces*, 2020, **12**, 19655–19663.

46 N. L. Chen, Y. Song, T. Lee, S. Mayarambakam and H. E. Katz, *J. Mater. Chem. A*, 2023, **11**, 17550–17559.

47 X. Shen, Y. Qi, M. Yuan, D. Chen, Y. Wang, Y. Sun and G. Shi, *Sci. Rep.*, 2025, **15**, 26831.

48 Q. Zhou, H. Li, C. Du, Z. Ye, L. Liang and G. Chen, *Nano Energy*, 2023, **118**, 109007.

49 S. A. Yamini, R. Santos, R. Fortulan, A. A. Gazder, A. Malhotra, D. Vashaee, I. Serhiienko and T. Mori, *ACS Appl. Mater. Interfaces*, 2023, **15**, 19220–19229.

50 V. Leonov, *IEEE Sens. J.*, 2013, **13**, 2284–2291.

51 D. Nam, G. Lee and J. Kim, *J. Ind. Eng. Chem.*, 2023, **123**, 201–208.